PROCEEDINGS OF THE ROYAL SOCIETY A

rspa.royalsocietypublishing.org

Research

Cite this article: Wang J, Liu C, Ma D. 2014 Experimental study of transport of a dimer on a vertically oscillating plate. *Proc. R. Soc. A* **470**: 20140439.
http://dx.doi.org/10.1098/rspa.2014.0439

Received: 4 June 2014
Accepted: 21 August 2014

Subject Areas:
mechanical engineering, mechanics

Keywords:
granular systems, multiple impacts, friction, nonlinear dynamics

Author for correspondence:
Caishan Liu
e-mail: liucs@pku.edu.cn

Electronic supplementary material is available at http://dx.doi.org/10.1098/rspa.2014.0439 or via http://rspa.royalsocietypublishing.org.

Royal Society Publishing

Experimental study of transport of a dimer on a vertically oscillating plate

Jiao Wang, Caishan Liu and Daolin Ma

State Key Laboratory for Turbulence and Complex Systems, College of Engineering, Peking University, Beijing 100871, People's Republic of China

It has recently been shown that a dimer, composed of two identical spheres rigidly connected by a rod, under harmonic vertical vibration can exhibit a self-ordered transport behaviour. In this case, the mass centre of the dimer will perform a circular orbit in the horizontal plane, or a straight line if confined between parallel walls. In order to validate the numerical discoveries, we experimentally investigate the temporal evolution of the dimer's motion in both two- and three-dimensional situations. A stereoscopic vision method with a pair of high-speed cameras is adopted to perform omnidirectional measurements. All the cases studied in our experiments are also simulated using an existing numerical model. The combined investigations detail the dimer's dynamics and clearly show that its transport behaviours originate from a series of combinations of different contact states. This series is critical to our understanding of the transport properties in the dimer's motion and related self-ordered phenomena in granular systems.

1. Introduction

Granular material under vibration sustains its motion by continually extracting energy from external environment. As an equilibrium state maintained via impacts and friction is reached, it usually presents complicated, yet self-ordered phenomena, such as the formation of large vortices [1,2], cluster phenomena [3], ordered separation [4,5], localized fluidization [6,7], etc. Similar phenomena can also be found in vibration conveyors and other mechanical systems subject to vibration [8]. Although scientific interests in these intriguing phenomena have

© 2014 The Author(s) Published by the Royal Society. All rights reserved.

sustained for several decades, the problem of how to characterize the underlying mechanism still remains open.

Exploring the underlying mechanism requires not only phenomenological analysis via a variety of experimental observations, but also a suitable numerical model for checking the variation of properties over ranges that could not always be explored experimentally. Most often, the dynamics of granular systems is studied via an idealized particle model without taking account the effects from particle geometry [9–13]. Despite the success of the simple model in explaining certain physical phenomena, recent studies have revealed that some anomalous phenomena are closely related to the shape of particles [14]. This motivates researchers to numerically and experimentally study the granular systems with particles in asymmetric geometry [2,14].

A dimer, that consists of two identical spheres rigidly connected by a light rod, is a typical object reflecting the influence from the particle shape on its dynamic properties. By releasing a dimer upon a vertically oscillating plate, many authors [15–19] have numerically and experimentally investigated its dynamical behaviours. Among them, Dorbolo *et al.* [19] presented impressive experimental results focusing on the planar dynamics of the dimer's motion. Depending on initial and driving conditions, the system exhibits various periodic responses that can be classified into three modes: *drift*, *jump* and *flutter*. In addition, the motion in a drift mode can be further classified into a negative or positive pattern, corresponding to the horizontal transport directed from the *bouncing ball* to the *staying ball*, or oppositely.

Different from an idealized particle, a dimer bounces upon a vibrating plate by experiencing frictional impacts occurring either at a single end or at both ends of the dimer. In these cases, the solutions of post-impact response cannot be directly obtained using a coefficient of restitution, yet require a sophisticated model to capture the dissipation and dispersion of energy evolving within the impact dynamics. Recently, we have developed a method [20] to solve these complex impact events, and have found successful applications for it in a variety of systems [21–24]. The theoretical development in understanding the dynamics of frictional impacts paves the way of characterizing the physical mechanism underlying the self-organized behaviours in the dimer system.

Inspired by the interesting phenomena of a two-dimensional dimer system [19], we recently adopted the method in [20] to model a three-dimensional bouncing dimer [25]. Our numerical results indicated that the normal motion of the three-dimensional dimer could have the same three modes as discovered for the two-dimensional version, whereas the mass centre of the dimer would follow distinct trajectories. In a *drift mode* of the three-dimensional motion, the trajectory of the mass centre projected onto a horizontal plane reveals either a *circular* or *spiral-inward* orbit, depending on the friction behaviours during a crucial event of *double impacts* (DIs). If friction at the end of the *staying ball* can enter into a *stick state*, a circular orbit will be formed in the three-dimensional drift mode. Otherwise, a spiral-inward orbit will appear.

Focusing attention on the *circular orbit* in a three-dimensional drift mode, we have performed systematic simulations [26] and found many characteristics exhibited in the circular orbit: its excitation depends on a proper combination of the values of Γ (the vibration intensity related to its frequency and amplitude) and e (the coefficient of restitution in impacts); both the orbit's radius and period are approximately proportional to the square of the frequency of vibration and the cube of the distance between the centres of the dimer's two spheres; the horizontal velocity initially specified to the dimer has just a small effect on the orbit shape.

Although the numerical simulations have revealed interesting results, these numerical phenomena are trustworthy only if they can be validated experimentally. Moreover, further quantification of the transport mechanism will certainly benefit from a validated numerical model with the ability to expose its dynamics in detail. In this paper, we will provide comprehensive experimental investigations for the dimer dynamics in both two- and three-dimensional scenarios. In our experiments, a vibration generator with a feedback controller is used to provide a stable oscillating signal. Four dimers with different sizes are tested under the external vibration with different driving parameters. We use a pair of high-speed cameras

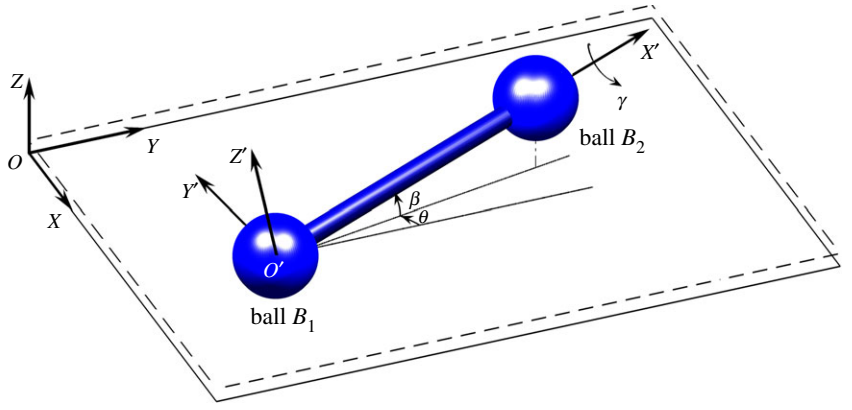

Figure 1. A dimer bouncing upon a plate undergoing a vertical oscillation. (Online version in colour.)

to sample the images of the dimers in motion. The kinematical quantities related to the degrees of freedom are then identified through a well-established image processing algorithm with enough measurement accuracy. By changing the initial and driving conditions, we also experimentally investigate their effects on the periodic behaviours of the dimer's drift motion.

Besides the experimental investigations, we also simulate all the cases studied in experiments. Not only are good agreements achieved between them, but also the transport properties discovered numerically are validated in our experiments. The combined investigations of simulations and experiments describe the dimer's dynamics in detail, and therefore may shed light on the underlying mechanism in a variety of the intriguing phenomena of granular systems.

The rest of this paper is organized as follows: §2 presents a brief description for the dimer system with contact and impact processes. In §3, we introduce the experimental apparatus and the measurement methods. Experimental realizations and comparisons between experimental and numerical results are performed in §§4 and 5 for the drift modes in two- and three-dimensional situations, respectively. Conclusion ends the paper in §6.

2. Brief description for the dynamics of the dimer system

Figure 1 shows a dimer bouncing upon a vertically oscillating plate. The dimer has two identical balls with mass m_b and radius r, rigidly connected by a rod with mass m_r, diameter D_r, and length $(l-2r)$, where l is the distance between the centres of the two balls. We designate B_1 and B_2 as the *staying ball* and *bouncing ball*, respectively. As the dimer moves in a *drift mode*, the bouncing height of B_2 is always larger than that of B_1.

The plate undergoes a vertically oscillating motion with amplitude A_z and angular frequency ω. At time t the distance of the plate from its equilibrium position takes the form $z_p = A_z \sin(\omega t + \phi_0)$, where ϕ_0 is the initial phase of the vibration at $t=0$. Following Dorbolo *et al.* [19], we define an aspect ratio $A_r = (l+2r)/(2r)$ along with r to describe the dimer's geometry, and a dimensionless acceleration $\Gamma = 4\pi^2 f^2 A_z/g$ along with $f = \omega/2\pi$ to represent the vibration intensity, where g is the gravitational acceleration. It is worth noting that the aspect ratio is closely related to the so-called kinetic angle between unilateral constraints, as defined in [27].

Designate (O, XYZ) as an inertial coordinate frame with the XY-plane corresponding to the equilibrium position of the vibrating plate. On this frame, the centres of B_1, B_2, and the rod are located at (x_1, y_1, z_1), (x_2, y_2, z_2), and (x_r, y_r, z_r), respectively. In order to give an attitude representation for the dimer, we establish a body-fixed coordinate frame $(O', X'Y'Z')$ fixed at the centre of B_1. Angle β between axis $O'X'$ and its projection on the horizontal plane is termed a *dip* angle, while θ between the oY-axis in the inertial frame and the projection of $O'X'$ on the horizontal plane is defined as a *precession* angle. Angle γ is related to the spinning motion of the

Table 1. Contact states possibly triggered in the motion of the bouncing dimer.

free motion	FM
contact at a single end	SC_{sk}, SC_{sp}
contact at both ends	$DC_{(sp,sp)}$, $DC_{(sk,sk)}$, $DC_{(sk,sp)}$, $DC_{(sp,sk)}$
impact at a single end	SI_{sk}, SI_{sp}
impact at both ends	$DI_{(sp,sp)}$, $DI_{(sp,sk)}$, $DI_{(sk,sk)}$, $DI_{(sk,sp)}$

dimer around $O'X'$. The rigid dimer possess six degrees of freedom which can be described by the generalized coordinates selected as $\mathbf{q} = (x_1, y_1, z_1, \theta, \beta, \gamma)^{\mathrm{T}} \in \mathbb{R}^6$.

We denote the instantaneous possible contact/impact point as p_1 on ball B_1 and p_2 on ball B_2. As far as interaction (impact or contact) is triggered, friction always satisfies Coulomb's friction law. To describe the interaction at each contact $p_i (i = 1, 2)$ under Coulomb friction, we decompose the contact force along its normal and two orthogonal tangential directions, and aggregate the normal and tangential components at the two contacts separately: $\boldsymbol{F}^n = [F_1^n, F_2^n]^{\mathrm{T}}$ and $\boldsymbol{F}^\tau = [F_{1x}^\tau, F_{2x}^\tau, F_{1y}^\tau, F_{2y}^\tau]^{\mathrm{T}}$. Using the Euler–Lagrange equations, we obtain the system dynamics as follows:

$$\boldsymbol{M}(\mathbf{q})\ddot{\mathbf{q}} - \boldsymbol{h}(\mathbf{q}, \dot{\mathbf{q}}, t) = \mathbf{Q}(\mathbf{q}) + \boldsymbol{W}(\mathbf{q})\boldsymbol{F}^n + \boldsymbol{N}(\mathbf{q})\boldsymbol{F}^\tau, \tag{2.1}$$

where the concrete expressions for mass matrix $\boldsymbol{M}(\mathbf{q})$, inertial–force matrix $\boldsymbol{h}(\mathbf{q}, \dot{\mathbf{q}}, t)$, gravity-induced matrix $\mathbf{Q}(\mathbf{q})$, and two Jacobian matrices $\boldsymbol{W}(\mathbf{q})$ and $\boldsymbol{N}(\mathbf{q})$ are referred to appendix A. In order to solve equation (2.1), the *contact state* of the dimer, which is related to the relative motion at each contact point p_i against the plate's motion, should be distinguished correctly. Table 1 shows the possible contact states that may be involved in the dimer's motion.

The meaning of symbol word marking in table 1 is as follows: FM stands for a free motion as both p_1 and p_2 are free in air; 'SC' means that a single contact is sustained either at p_1 or p_2; 'SI' represents that a single impact occurs either at p_1 or p_2 while the other one is airborne. For the symbol words whose first character is 'D' (implying 'double'), these contact states mean that both points p_1 and p_2 have interactions with the plate. 'DC' is a state in which both p_1 and p_2 contact the plate simultaneously; 'DI' represents a state of 'double impacts', corresponding to the cases of one ball colliding with the plate while the other one is either contacting or simultaneously colliding with the plate. Subscripts in these capital symbol words represent the friction state at the corresponding contact points p_1 and p_2: 'sk' for stick, and 'sp' for slip.

For the dimer's motion in a contact state 'SC', or 'DC', the normal interaction at a sustained contact point p_i is modelled as a normal constraint established through the relative kinematics at the contact point. By the normal constraint equation, together with the friction relationship, we can use an LCP formulation [8,23] to uniquely determine the contact forces $\boldsymbol{F}^n$ and $\boldsymbol{F}^\tau$, except for certain singular situations that need special treatments [25].

Impacts occur when the dimer is in a contact state 'SI' or 'DI'. In these cases, the momentum and energy within the dimer will evolve quickly due to the strong interaction at the impact sites. In order to avoid unnecessary digression, we refer for the details for modelling these impact events to [20,25,26].

3. Experimental set-up, physical parameters and measurement methods

Experiments are conducted in an experimental apparatus consisting of a vibration generator (ES-6), a plate made of duralumin, and two high-speed cameras (Lavision HighSpeedStar 4G). Figure 2 shows a schematic of the experimental system. The duralumin plate in a size of $100 \times 60 \times 4$ cm is firmly fixed on the vibration generator by 16 hexagonal nuts (17-M8). An accelerator (B&K4386) is glued on the surface of the duralumin plate to measure its acceleration. With a feedback controller, the plate vertically oscillates following a harmonic signal with given values of parameters Γ and f.

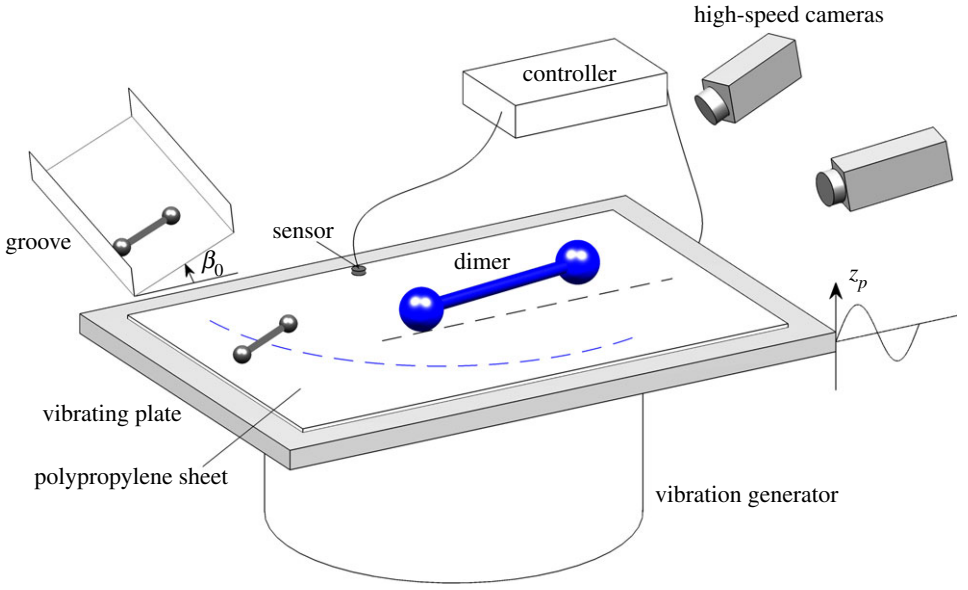

Figure 2. Schematic of the experimental equipment for testing dimer motion. (Online version in colour.)

Table 2. Material and geometrical parameters of dimers.

dimer	drift	(ρ_b^a, ρ_r^b)(kg m^{-3})	r (mm)	l (mm)	A_r	D_r (mm)
D-I	2D	$(7.85, 1.18) \times 10^3$	8.75	66.28	4.8	6.20
D-II	2D	$(7.85, 1.18) \times 10^3$	8.75	110.10	7.3	6.20
D-III	2D	$(7.85, 1.18) \times 10^3$	8.75	152.79	9.7	6.20
D-IV	3D	$(7.85, 7.85) \times 10^3$	2.00	11.94	4.0	2.34

[a] ρ_b denotes material density of the balls.
[b] ρ_r denotes material density of the rod.

Four dimers with different shapes are separately tested in our experiments. Table 2 presents the parameters relative to the geometry and material properties of the four dimers. Three of them, designated as D-I, D-II and D-III, are fabricated with identical steel balls rigidly connected by a polyester plastic rod with length changed to give different aspect ratio, $A_r = l/(2r) + 1$. Without any additional physical limitation, the motion of these three dimers can enter into a two-dimensional scenario by an initial condition described as follows [19]: the *bouncing ball* is lifted by a fraction of the ball diameter, then it is released while keeping the *staying ball* on the plate.

The remaining one, designated as D-IV, is used for three-dimensional investigation. This dimer is machined into shape from a piece of steel rod with the same material as the one of the balls in other three dimers. To trigger a three-dimensional motion, the dimer is initially set on a U-shaped groove with a flat bottom inclined with angles to both the vertical and horizontal planes. The inclined angle to the horizontal plane is set as $\beta_0 \approx 30^\circ$, and the angle to the vertical plane is small enough to allow the dimer to roll on the groove along a nearly straight line trajectory. The groove is at a small distance above the plate for collision avoidance in vibration.

Previous numerical investigations [26] have indicated that the excitation of a drift mode strictly depends on a proper combination of the vibration intensity Γ and the coefficient of restitution e. In addition, the horizontal transport behaviours are also influenced by the values of the friction coefficients. In order to find a suitable contact interface with proper physical properties that could satisfy our experimental requirements, we covered the duralumin plate with either a smooth

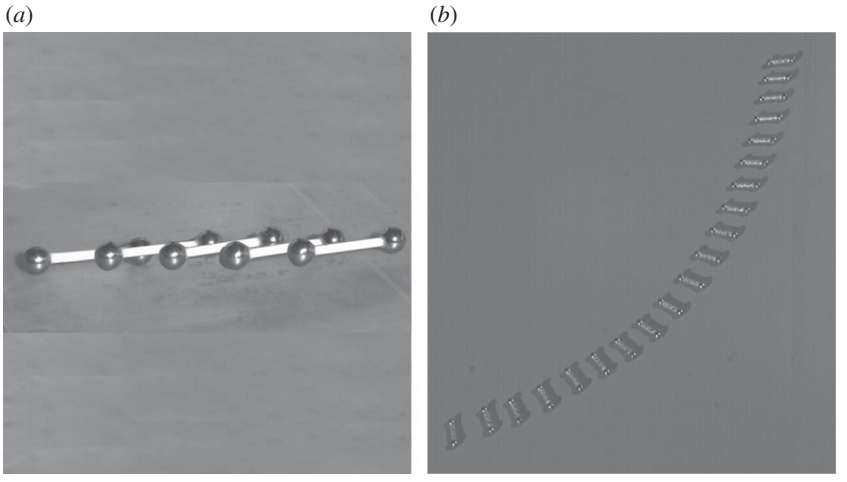

Figure 3. Typical sequence of (*a*) dimer D-I in a two-dimensional drift mode and (*b*) dimer D-IV in a three-dimensional drift mode.

Table 3. Impact and friction parameters related to the two interfaces of the vibrating plate.

interface	drift	e	$(\mu, \mu^s)^a$	$(\mu_I, \mu_I^s)^b$
sheet-I	2D	0.52	(0.08, 0.15)	(0.05, 0.15)
sheet-II	3D	0.6	(0.4, 0.8)	(0.25, 0.8)

[a]Slip and stick coefficients of friction in contact.
[b]Slip and stick coefficients of friction in impact.

polypropylene plastic sheet (Sheet-I) or a rough polypropylene plastic sheet (Sheet-II). The three dimers (D-I, D-II and D-III) are tested separately on the same surface of Sheet-I. Under the contact surface, we expect to observe both positive and negative drift patterns along with the variation in the shapes of the three dimers. Dimer D-IV is tested over the contact surface Sheet-II. This surface provides large friction with coefficients whose values are greater than the necessary ones for sustaining the mass centre of dimer D-IV to perform a circular orbit.[1]

Table 3 presents the parameters in impact and friction used in numerical investigations. The coefficients of restitution are determined from experiments of releasing an independent steel ball, as the one same in dimer D-I, onto the plate covered with Sheet-I or Sheet-II, separately. The coefficients of friction are estimated via a fitting method to find their best values. As demonstrated in the existing experiments given by Dorbolo *et al.* in [19], impacts change the sliding coefficient of friction and make it different from the one in contacts. Here, we also assign different values for the sliding coefficients of the friction in the contact and impact processes, separately.

The positions and attitudes of the dimer are measured using a stereoscopic vision method [28]. A pair of high-speed cameras are fixed to continuously record the dimer's motion. The orientations of the cameras are selected carefully so that the images of the dimer are formed in a good visual angle. The images are sampled by a frame rate of 1000 frames per second, with a resolution of 1024 × 1024 pixels. In the cases studied in our experiments, the dimer's motion is recorded by the two cameras as a stable drift mode is observed. Figure 3*a*,*b* presents a typical sequence of the trajectories of dimers D-I and D-IV in two- and three-dimensional drift modes, respectively.

[1]If the friction is not large enough, as numerically demonstrated in [26], the orbit will spiral inward even though a three-dimensional drift mode can be formed approximately.

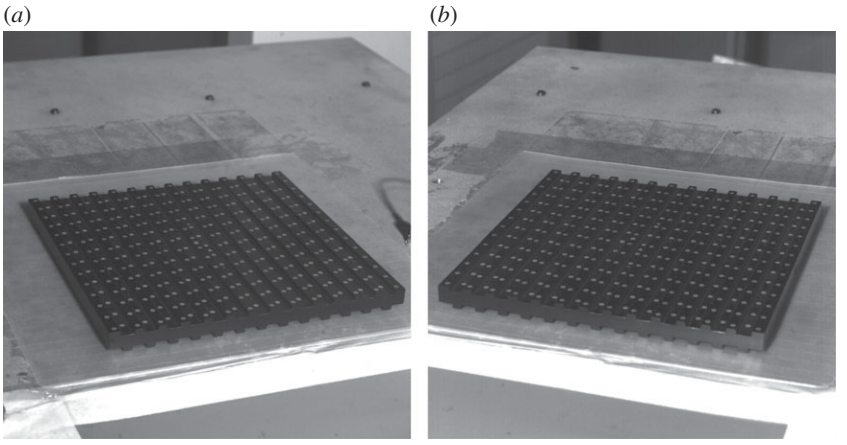

Figure 4. Images of a standard calibration board captured by two cameras at the same instant.

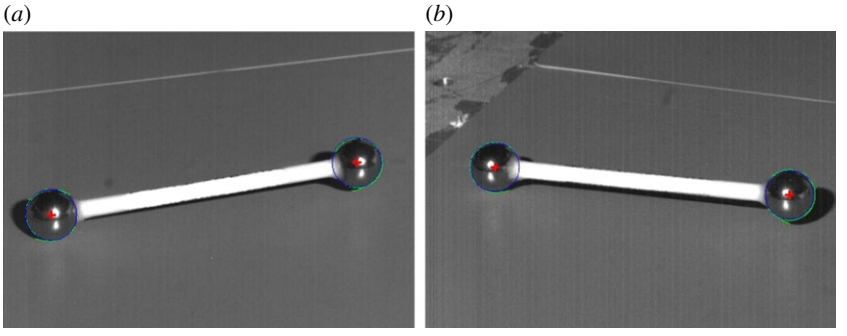

Figure 5. Two synchronous images of dimer D-I captured by two cameras at the same instant, superimposed by the reconstructed contours of both balls (circles). (Online version in colour.)

A pinhole camera model is used to describe the relation between a spatial point and its projection position in an image. We obtained the calibration information for the two CCD cameras by the method described in [29], in which a standard chessboard is used. Figure 4 shows two images of the calibration board captured by the two cameras at the same instant. Using an in-house software package based on a well-established image processing algorithm, we analyse the pictures of the chessboard over different orientations to determine the camera's matrices. The matrices contain the intrinsic parameters related to the focal length, the distortion parameters of the lenses, and the external parameters, such as the entries of the transition matrix between the pixel coordinate system fixed on the image and the inertial coordinate system fixed in space.

Based on the calibration information, we digitize the current dimer's configuration using pairs of images captured at the same instant. Figure 5 shows two images of dimer D-I synchronously captured by the two cameras, overlapped by the reconstructed contours of the balls obtained via the image analysis. Since the images provide no recognizable markers to effectively distinguish the spinning rotation, only five degrees of freedom of the dimer are identified by our image processing algorithm. They are the coordinates of the mass centre of the dimer (x_r, y_r, z_r) and the precession angle θ and dip angle β.

By the stereoscopic vision method, all the variables describing the three degrees of freedom in two-dimensional motion can always be identified via image analysis. In two-dimensional experiments, our numerical algorithm in the data processing may generate a recognition error

of about 0.5 pixel. According to the calibration information, one image pixel corresponds to a distance in space with a value about 0.2 mm. So, the position error is estimated with a value about $0.5 \times 0.2 = 0.1$ mm. Since angular variable β is basically computed through the position information of the two balls, its error varies with the dimer's sizes, and decreases along with increasing the rod length. The errors of β for dimers D-I, D-II and D-III are about 0.0024, 0.0015 and 0.0012 rad, respectively. The relative errors in two-dimensional experiments are all within 5%.

For effectively tracing the trajectory of three-dimensional motion, we have to set the two cameras with large view fields. The enlarged view fields reduce the measurement accuracy to a certain extent. In our three-dimensional experiments, the calibration information indicated that one pixel in an image is associated with a distance of about 0.8 mm. In addition, the small size in D-IV also makes image recognition generate a relative large error near one *pixel*. Therefore, the measurement accuracy in three-dimensional experiments is estimated with a position error of about 0.8 mm, up to 40% of the regular value of the vertical displacement $z_r(t)$. Relative large errors also exist in identifying angular variables $\theta(t)$ and $\beta(t)$. Therefore, the measured values for $z_r(t)$, $\theta(t)$ and $\beta(t)$ are basically untrustworthy. However, the measurement errors pollute little $x_r(t)$ and $y_r(t)$ since they are relatively large enough. In our three-dimensional experiments, only the measured values of $x_r(t)$ and $y_r(t)$ are taken as the valid outputs.

4. Two-dimensional drift mode

In this section, we will investigate the two-dimensional drift mode exhibited in dimers D-I, D-II and D-III, separately. Experimental investigations will be combined with numerical simulations to explore the details in the dimer's dynamics. Under the same driving parameters, the effect from dimer's shape on the transport behaviours will be studied. We will also change the initial and driving conditions to examine their effects on the transport behaviours.

(a) Details in the dynamics

By setting $\Gamma = 1.2$ and $f = 20$ Hz, we present the results for dimer D-I as an example to exhibit the details of the two-dimensional dimer's dynamics in a drift mode. For comparing with the experimental results, we perform numerical simulations by specifying the dimer with an initial condition as follows: $\mathbf{q}(0) = (0, 0, r + A_z \sin\phi_0, 0, \beta_0, 0)^{\mathrm{T}}$ and $\dot{\mathbf{q}}(0) = (0, 0, 0, 0, 0, 0)^{\mathrm{T}}$, where β_0 and ϕ_0 are, respectively, the initial values of the dip angle and the phase of the plate at the release time $t = 0$. This initial condition generally agrees with our experiment scenario for triggering a two-dimensional motion.

The excitation of a drift mode is sensitive to both the values of ϕ_0 and β_0. In particular, ϕ_0 is hardly controlled in the experiments of releasing the dimer by hand. As the initial configuration of a dimer remains unchanged approximately, several trials need to be performed for experimentally observing a stable drift motion. For activating a drift mode in simulations, β_0 can be roughly estimated through the images captured by two cameras, whereas a fitting method must be used to determine a proper value of ϕ_0, which is not unique but limited in a specific range.

Figure 6 presents the numerical and experimental results for the values of $\beta(t)$ and $\dot{\beta}(t)$. Numerical results are obtained by setting $\beta_0 = 4.9^\circ$ and $\phi_0 = 0.8151$ rad, together with the physical parameters given in tables 2 and 3. Both $\beta(t)$ and $\dot{\beta}(t)$ vary periodically accompanying the vibration, while $\dot{\beta}(t)$ jumps at each instant of $\beta(t) = 0$, corresponding to the instant when an event of *DIs* occurs. The same phenomenon can also be numerically obtained when ϕ_0 varies with values near to $\phi_0 = 0.8151$ rad.

The experimental curve of $\dot{\beta}(t)$ is obtained by an eulerian difference method. Since this difference method is basically sensitive to the measurement error existing in the values of $\beta(t)$, good agreement between the computed and measured curves of $\dot{\beta}(t)$ in figure 6 means that our measurement method provides sufficiently accurate data.

In order to reveal the phase of the plate at the instant for the occurrence of *DIs*, figure 7 shows the curves of the measured and computed $z_r(t)$, superimposed by the curve of the harmonic signal

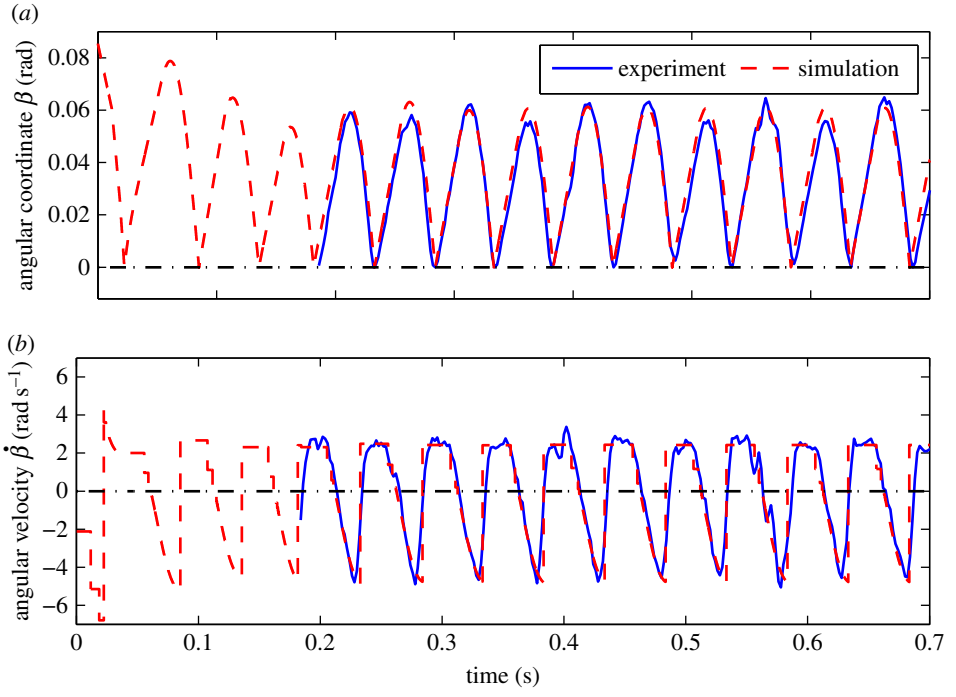

Figure 6. Experimental and numerical results of: (*a*) dip angle β and (*b*) the angular velocity $\dot{\beta}$, for dimer D-I. $\Gamma = 1.2$, $f = 20$ Hz, $\beta_0 = 4.9^\circ$, $\phi_0 = 0.8151$. (Online version in colour.)

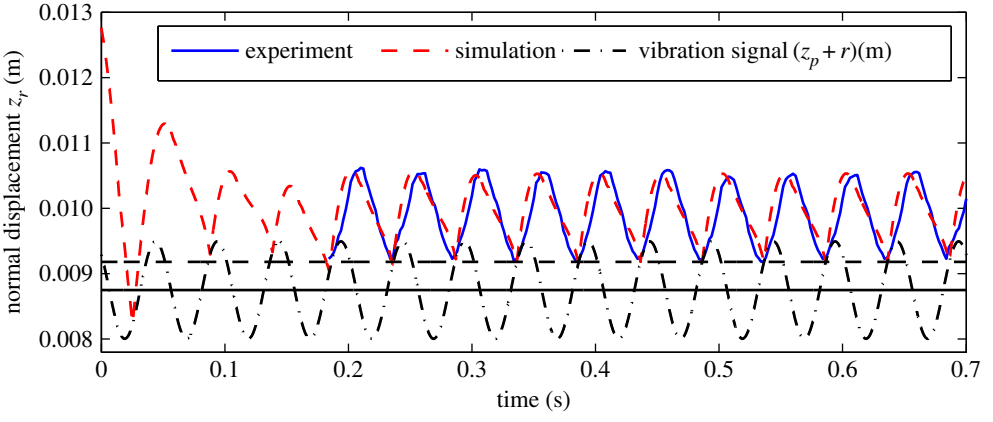

Figure 7. Normal displacement $z_r(t)$ of dimer D-I: $\Gamma = 1.2$, $f = 20$ Hz, $\beta_0 = 4.9^\circ$ and $\phi_0 = 0.8151$. Solid black line stands for the equilibrium position of the vibration signal after translation. (Online version in colour.)

$z_p(t)$. In this figure, we translate curve $z_p(t)$ onto a position apart from its equilibrium position with a distance equal to the radius of the sphere ($r = 8.75$ mm). The intersection points between the curves of $z_r(t)$ and $(z_p(t) + r)$ mark the sequence of the DIs. It is clear that the sequence corresponds to a fixed phase that appears in the first quadrant of the z_p–$\dot{z}_p$ plane. Therefore, we may say that the event of DIs reveals a *phase-locking phenomenon*. As the event occurs, the direction of the pre-impact normal velocity at the bouncing end of the dimer is always opposite to that of the vibrating velocity of the plate, such that part of energy within the vibration is transferred to the dimer.

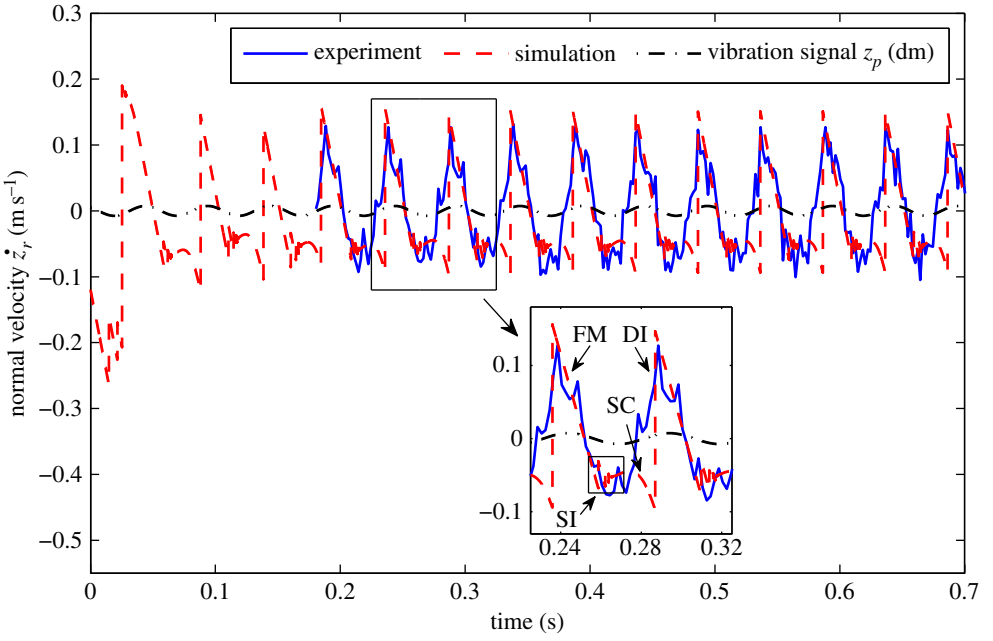

Figure 8. Normal velocity $\dot{z}_r(t)$ for dimer D-I: $\Gamma = 1.2, f = 20$ Hz, $\beta_0 = 4.9^\circ$ and $\phi_0 = 0.8151$. Inset details the contact states during a cycle of the drift mode. (Online version in colour.)

Besides the crucial event of DIs, other contact states, such as 'FM', 'SI' and 'SC' exist in every cycle of the drift mode. Transitions among these contact states certainly bring on distinct behaviours in the dimer's motion. Relatively, the variables shown in figures 6 and 7 are insensitivity to the transitions among other contact states, except the DIs. For conveniently detailing the evolution of the contact state within the dimer dynamics, figure 8 plots the numerical and experimental curves of $\dot{z}_r(t)$. Here, we obtain the experimental values of $\dot{z}_r(t)$ using a piecewise difference method to treat the measured values of $z_r(t)$. Namely, the instants related to the events of DIs are firstly distinguished according to experimental data, then an eulerian difference method is adopted to treat the data between two subsequent events of the double impacts.[2]

By the inset in figure 8, we can clearly find that the contact states within a cycle of the vibration evolve as follows: the dimer begins with a free motion, followed by a sequence of SIs at the end of *staying ball*, then the sequence transfers into a contact mode at the *staying ball* while the *bouncing ball* still stays in air. The cycle ends with an event of DIs when the *bouncing ball* lands onto the plate.

(b) Effect of initial states on drift velocity

As numerically demonstrated in [26], the same drift mode can be excited by different initial states scattering in a sequence of sets scaled by the initial variable β_0. To examine this numerical prediction, figure 9 shows a group of curves for the horizontal displacement $y_r(t)$ of dimer D-I versus the number of T, where $T = 1/f$ is the period of the vibration. These curves are obtained from the drift modes of dimer D-I under five different initial configurations β_0 with the same driving parameters $\Gamma = 1.2$ and $f = 20$ Hz. To observe a stable drift mode for each β_0, several

[2]The discrepancy in the curves of figure 8 comes from the experimental data processing, the uncertainty in our experiment measurements, and the model error induced by the numerical model in which the small scale in the time interval of impacts is ignored completely.

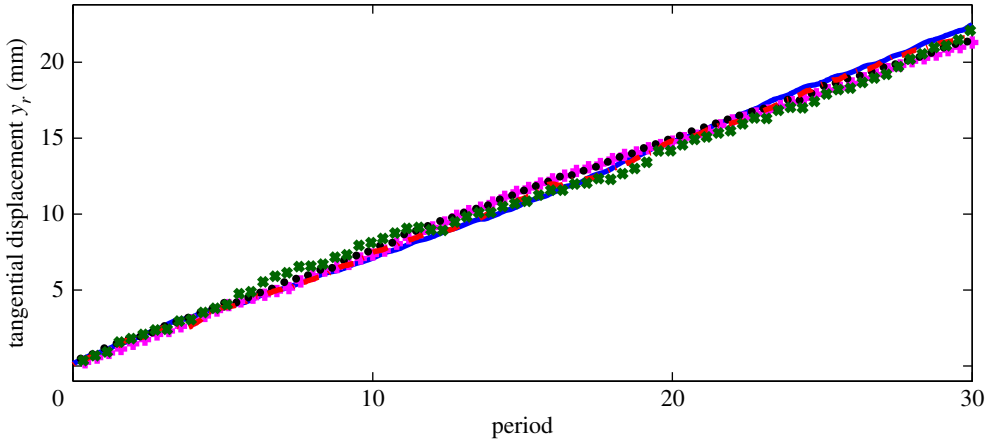

Figure 9. Horizontal displacement $y_r(t)$ versus the number of periods T for D-I starting its motion under an initial configuration, $\beta_0 = 3.2^\circ, 4.9^\circ, 5.4^\circ, 6.3^\circ, 7.1^\circ$, respectively. $\Gamma = 1.2$, $f = 20$ Hz. (Online version in colour.)

trials are needed by releasing the dimer at an instant when the plate is in a proper phase ϕ_0. As shown in figure 9, the same drift mode is observed in these five experiments. In the following, comparisons between our numerical and experimental results will be given without the concrete illustration for the initial states specified to the numerical simulations.

(c) Effect of dimer's geometry on drift velocity

Dorbolo *et al.* [19] thoroughly studied the effects of dimer's shape on the transport behaviours. They found that the changes in dimer's shape may result in different drift modes classified into a negative or positive pattern. Namely, the horizontal transport is directed either from the *bouncing ball* to the *staying ball*, or oppositely. The mechanism underlying these distinct horizontal behaviours was explained by Zhao *et al.* [21] via numerical simulations. Here, we supplement more information through numerically and experimentally investigating the drift motions in dimers D-I, D-II and D-III, separately.

Under $\Gamma = 1.2$ and $f = 20$ Hz, all the three dimers can enter into a drift motion by properly selecting initial states. Figure 10 presents both the numerical and experimental results of $y_r(t)$ within a time interval of $30\,T$, where $y_r(t)$ is the horizontal displacement of the mass centre of the dimer. Noise in these curves comes from the periodical fluctuation during transports and the measurement errors. Good agreements are achieved for each dimer in the comparison of its numerical and experimental results. Moreover, the three dimers exhibit different transport behaviours: dimers D-I and D-II transport positively with a velocity decreasing with increasing the rod length, whereas D-III transports in a negative direction. The electronic supplementary material provides movies demonstrating the different drift motions.

There is no doubt that friction should be responsible for the occurrence of the horizontal transport behaviours. Understanding the friction behaviours in the dimer motion requires the information of the horizontal velocities at the contacting points. Following Dorbolo *et al.* [19], we plot in figure 12 the curves of $\upsilon_{1y}^{\tau}(t)$ for dimers D-I and D-III, separately. Here, $\upsilon_{1y}^{\tau}(t)$ represents the horizontal component of the simultaneous velocity at contact point p_1 that always located at the bottom of the *staying ball* B_1. Since the point moves on to the surface of the ball as the dimer rotates, the values of $\upsilon_{1y}^{\tau}(t)$ are obtained by a kinematical relationship treating the observed and calculated data in experiments and simulations [25], respectively.

Besides good agreements between our numerical and experimental results, the curves in figure 11 show two kinds of asymmetric structures. Let us consider the curves within a single

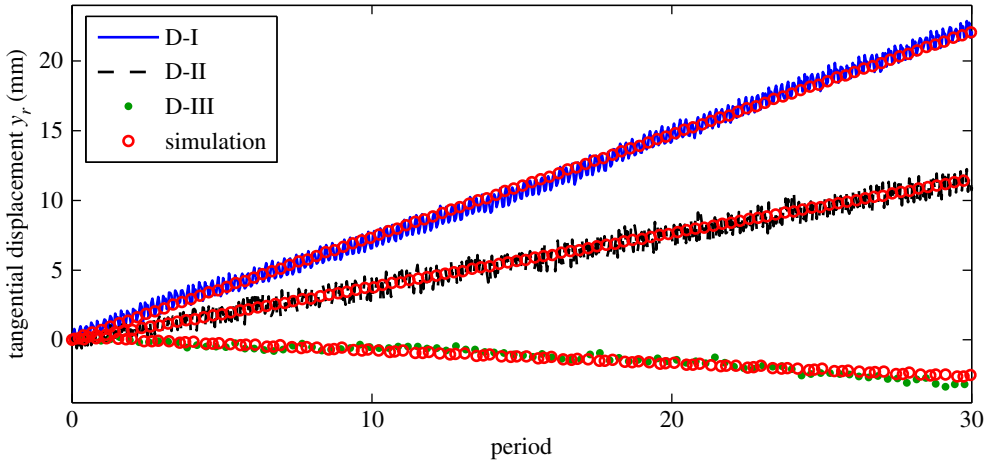

Figure 10. Horizontal displacements $y_r(t)$ passed by D-I ($A_r = 4.8$), D-II ($A_r = 7.3$) and D-III ($A_r = 9.7$) within 30 T. $\Gamma = 1.2$, $f = 20$ Hz. (Online version in colour.)

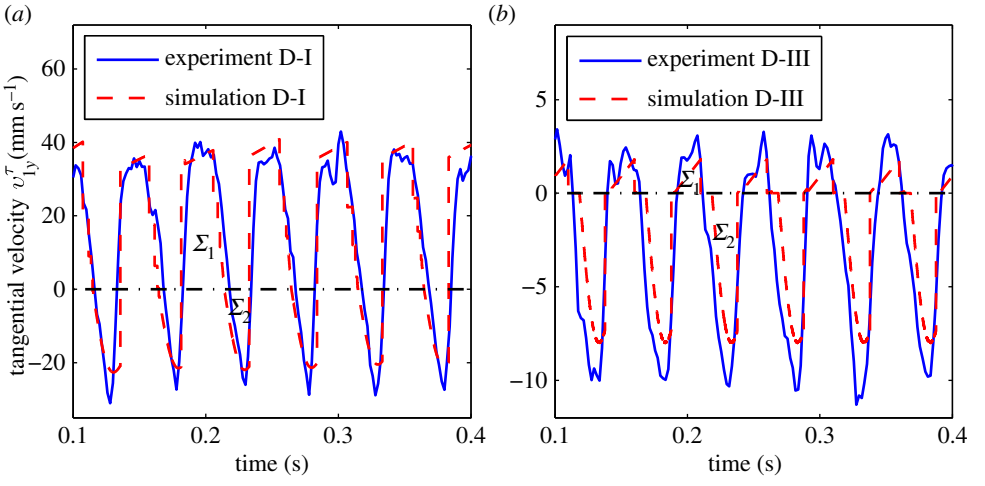

Figure 11. Curves extracted from experimental and numerical results of $v_{1y}^{\tau}(t)$ appearing in (*a*) D-I and (*b*) D-III. $\Gamma = 1.2$, $f = 20$ Hz. (Online version in colour.)

cycle of the vibration, and designate Σ_1 and Σ_2 as the areas enclosed by its positive and negative parts, respectively. The structure in D-I corresponds to $\Sigma_1 > \Sigma_2$, whereas the one in D-III is in an opposite situation.

The probable reason for the formation of two kinds of the structures has been analysed in [21]. The main difference between them is related to the variation of friction state appearing in the process of DIs: the negative slip state of friction at contact point p_1 at the start of DIs changes into a stick and the positive slip state at the end of the DIs in D-III and D-I, respectively. By qualitatively analysing the dynamics of double impacts, Zhao *et al.* [21] gave a statement as follows: a stick state can be involved in double impacts if $\mu_s^I > mrl/(2(J_1 + mr^2))$, where μ_s^I is the static coefficient of friction at p_1, m the total mass of the dimer and J_1 the moment of inertia with respect to the mass centre of the dimer. As the rod's mass is ignorable, this condition is simplified into a formula: $\mu_s^I > (A_r - 1)/(7/5 + (A_r - 1)^2)$, agreeing with the one given in [19]. Let us use this condition to

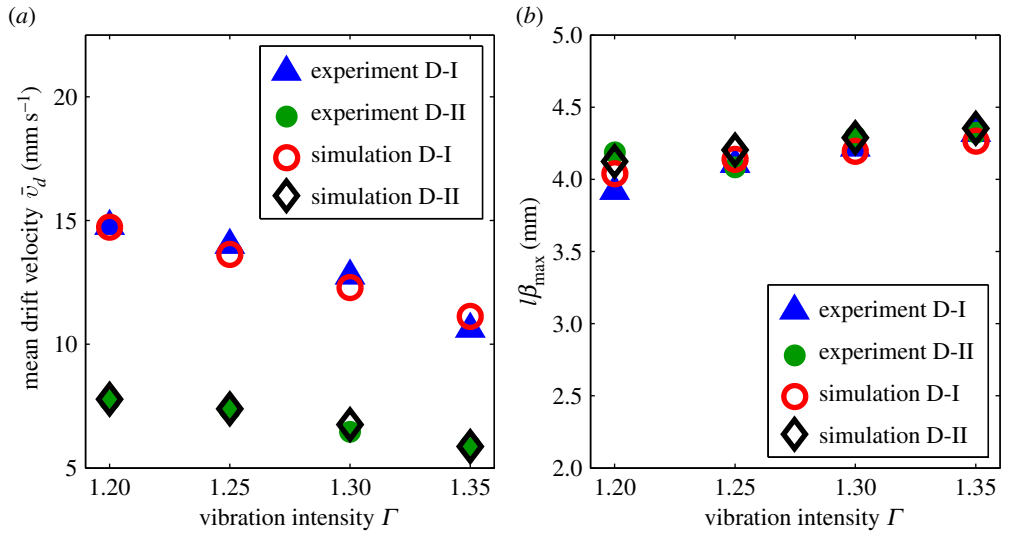

Figure 12. (*a*) The mean drift velocities $\bar{v}_d$ and (*b*) the maximum height of the bouncing end, versus Γ for D-I and D-II under $f = 20$ Hz. (Online version in colour.)

check the three tested dimers ($A_r = 4.7, 7.3, 9.8$). With the same $\mu_s^I = 0.16$, this condition can only be satisfied by D-III, so it drifts along a direction opposite to the one of other two dimers.[3]

When observing in the electronic supplementary material, video (see footnote 3), we can find that the connecting rod in D-III slightly bends accompanying its drift motion. The cause of the physical phenomenon is partly due to the flexibility of the rod as it has a long length, and is also due to the stick state occurring in the event of double impacts. The appearance of the stick state in the end of the *contacting ball* allows the rod to manifest low-order bending mode when the *bouncing ball* is detached from the plate. Owing to the rod flexibility in D-III, figure 11*b* reveals that there is a relative large discrepancy between the numerical and experimental results. Nevertheless, this factor has little effect on the quantities describing the global horizontal transport. See, e.g. figure 10.

(d) Effects of driving parameters on drift motion

Besides dimer's geometry, the driving parameters in vibration also influence the transport property. In [26], we have numerically found that the excitation of a drift mode would strictly depend on a proper combination of the vibration intensity Γ and the coefficient of restitution e. For a given e, the drift mode can be excited only if the value of Γ is limited in a specific range. Under the same intensity Γ and the same coefficient of restitution e, the experimental results [19] given by Dorbolo *et al.* have revealed that the mean drift velocity, designated as $\bar{v}_d$ here, is approximately inversely proportional to the driving frequency f. Nevertheless, the correlation between Γ and $\bar{v}_d$ was not quantitatively investigated in their experiments.

In the present paper, we perform our investigations just focusing on the effects of Γ over the transport property as dimers drift positively on the same contact surface. We test dimers D-I and D-II by setting the vibration with the same frequency $f = 20$ Hz, while limiting the value of Γ in a scope from 1.2 to 1.35. Under these driving parameters coupled with a proper initial state, and setting Sheet-I as the contact surface, both the dimers can enter into a positive drift mode.

[3]The amplitude and direction of the mean drift velocity essentially depend on the difference between areas Σ_1 and Σ_2. Even though no stick state appears in the process of DIs, a negative drift mode may also occur when a dimer with a suitable shape drifts on a surface with proper friction.

Figure 12*a* shows the values of the mean drift velocity $\bar{v}_d$ obtained by averaging the observed and computed values of $y_r(t)$ within $30\,T$. For all the cases of $\Gamma = 1.2, 1.25, 1.3$ and 1.35 under the same $f = 20\,\mathrm{Hz}$, both the numerical results of dimer D-I and D-II can agree with their corresponding experimental findings. By figure 12*a*, we can also find that for each dimer the value of $\bar{v}_d$ varies with the change of Γ.

(e) Energy confined in the normal motion

As has been demonstrated previously, the initial state has little effect on the transport property in two-dimensional experiments. Moreover, the event of DIs, corresponding to a scenario that the *bouncing ball* collides against the plate while the *staying ball* contacting the plate, plays a dominant role of extracting external energy to maintain a periodic drift mode. The normal motion of the dimer can then be approximately characterized by the impact behaviour of the *bouncing ball* during the crucial event of DIs. To illustrate this point, figure 12*b* shows the bouncing height $h_{\max} = l\beta_{\max}$ of the *bouncing ball* in dimers D-I and D-II under different driving conditions studied in our experiments.

Although the shapes between the two dimers are different, and Γ varies in a relative large range, the values of $h_{\max}$ in the studied cases change little. From this phenomenon, we may conjecture that the bouncing-dimer dynamics takes certain similarities in comparison with the fundamental bouncing-ball problem [9,12]. Note that there are many mature theoretical results existing in the bouncing-ball problem. This similarity may be beneficial to theoretically quantifying the physical mechanism underlying the transport behaviour of the dimer system.

5. Three-dimensional drift mode

In this section, we will experimentally investigate the three-dimensional drift dynamics by testing dimer D-IV moving on contact surface Sheet-II. Evolution of the contact state within the three-dimensional drift dynamics will be illustrated by the image frames captured by the high-speed camera. Under different initial and driving conditions, the circular orbit and related properties performed by the three-dimensional dimer will also be experimentally validated.

(a) Evolution of contact state in three-dimensional drift mode

Similar to the cases in the two-dimensional version, a three-dimensional drift mode within each cycle of the vibration also contains many different contact states that can be repeated periodically. To clearly expose the evolution of the contact states, we present in figure 13 the images that are captured at a sequence of instants in between with an equal time interval $(T + T/6)$. The sequence starts from an image frame t_i^{di} of a DI state in the ith cycle, following an image frame t_{i+1}^{fm} of a free-motion state (FM) in the next cycle, then an image frame t_{i+2}^{si} of a SI state in $(i+2)$th cycle. The SI at the *staying ball* continually occurs before the dimer's motion enters into an SC state, corresponding to the subsequent frames t_{i+3}^{sc}, t_{i+4}^{sc} and t_{i+5}^{sc}. After that, the *bouncing ball* comes back to the plate, and triggers a repeated DI state (image t_{i+6}^{di}). Besides the sequence of image frames, the electronic supplementary material also provides a movie demonstrating the three-dimensional drift motion.

(b) Effects of initial conditions on a circular orbit

We perform three-dimensional experiments in a scenario as follows: initially dimer D-IV is set by hand on the bottom of the inclined groove, and takes a configuration of its rod axis parallel to the bottom edge of the groove. After release, the dimer will first roll on the groove, then collide against the vibrating plate to trigger a three-dimensional motion.

Suppose that $\dot{x}_1(0)$ corresponds to the value of the horizontal velocity of the *staying ball* at the instant when it contacts the plate. We assign $\dot{x}_1(0)$ with different values to distinguish the

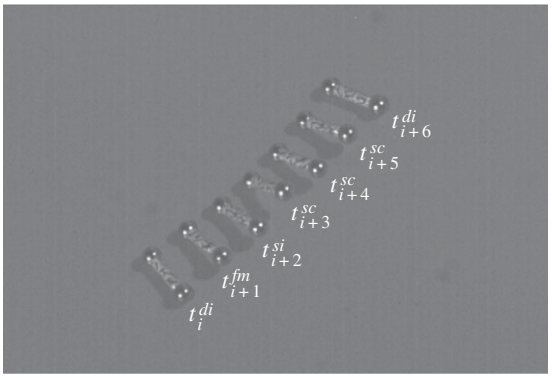

Figure 13. Evolution of contact state in a three-dimensional drift motion. $\Gamma = 1.0$, $f = 20$ Hz.

initial states of the dimer. In our experiments, we design five initial states, designated as C_j ($j = 1, 2, \ldots, 5$) as follows: the values of $\dot{x}_1(0)$ from cases C_1 to C_5 follow an arithmetical sequence with a common difference of $0.05\,\mathrm{m\,s^{-1}}$, starting from 0.2 to $0.4\,\mathrm{m\,s^{-1}}$. From each value of $\dot{x}_1(0)$, we estimate the initial position of the dimer lying on the groove, then release it to start a three-dimensional experiment.

All the cases from C_1 to C_5 are experimentally investigated under the same vibration with $\Gamma = 1.0$ and $f = 20$ Hz. Similar to two-dimensional experiments, for triggering a three-dimensional drift mode in case C_j, several trials are usually needed in order to make the plate with a proper phase at the instant when the dimer is released.

In terms of our numerical discoveries [26], the mass centre of the dimer in all the cases should perform a nearly same circular orbit. To validate this property, we calculate the circle template of each case C_j as follows: Suppose that the measured point $(x_r(t), y_r(t))$ is located in a circle with radius $\bar{R}_e$ and centre coordinates (X_C, Y_C), whose standard equation is expressed as

$$[2x_r(t),\ 2y_r(t),\ 1]\begin{bmatrix} X_c \\ Y_c \\ \bar{R}_e^2 - X_c^2 - Y_c^2 \end{bmatrix} = x_r^2(t) + y_r^2(t). \tag{5.1}$$

By (5.1), together with the experimental outputs in each tested case C_j, we can use a least square method to determine the values of X_c, Y_c and $\bar{R}_e$. If the circle template of C_j can be followed by the corresponding experimental data, and the values of $\bar{R}_e$ in all the tested cases are nearly the same, the property that the shape of the circular orbit is independent of the initial state can be confirmed.

Considering that translation and rotation operations do not change the shape of a circle, we translate all the experimental data into a coordinate system to make (X_C, Y_C) located at its origin. Then, we perform a rotation transform to make each experimental curve rotate a certain angle around the origin. After that, these experimental curves can be separately expressed on the different portion of a circle plane. Figure 14 shows the horizontal trajectories of the mass centre of the dimer in the five independent experimental cases, together with the corresponding radius $\bar{R}_e$ and the angle of circumference α. All of them are nearly located on a same circular orbit with radius $\bar{R}_e \approx 207$ mm, except the case C_3.

Case C_3 provides a suspicious result that deviates much from those in the other cases. We attribute the error to the mis-operation made in the experiment. The reason for that is explained as follows: The numerical discoveries in [26] have indicated that the radius $\bar{R}_e$ is approximately proportional to f^2. As $f = 20$ Hz corresponds to a radius with a correct value of $\bar{R}_e \approx 207$ mm, the measured value of $\bar{R}_e \approx 186$ mm in case C_3 should correspond to a frequency $f = 19$ Hz. Therefore, a mistake of assigning an incorrect value of frequency to the vibration

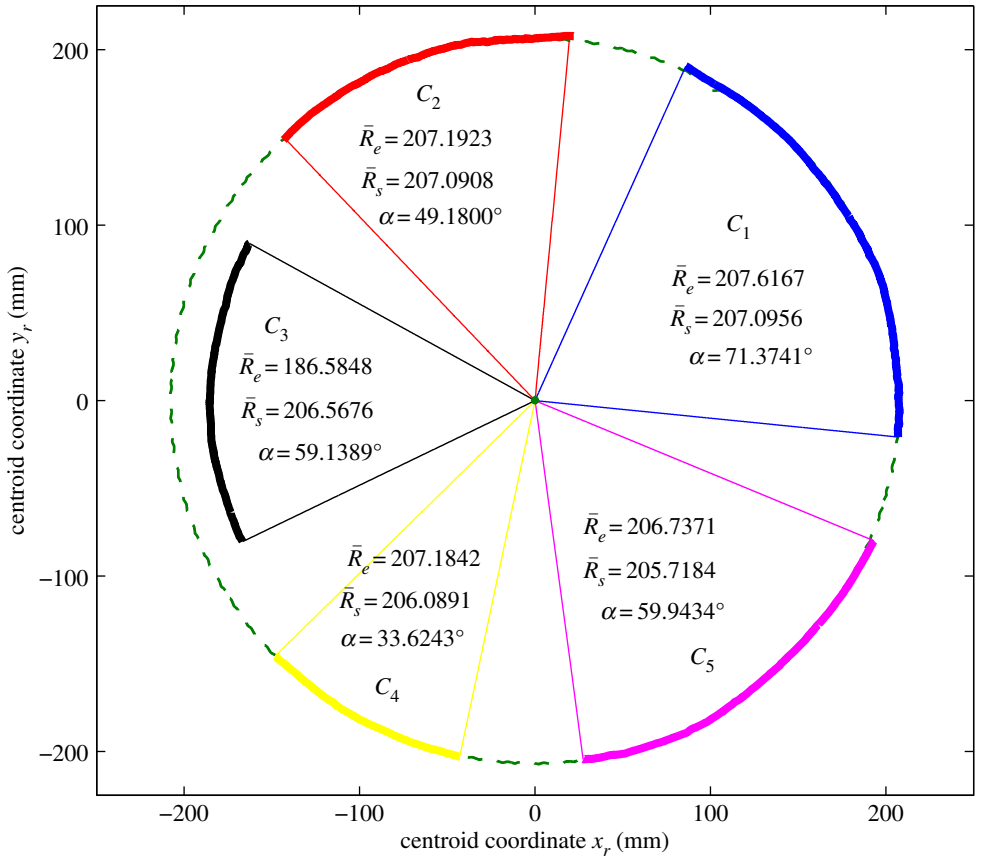

Figure 14. Horizontal trajectories of the mass centre of dimer D-IV in five different initial states from case C_1 to C_5 under the same vibration: $\Gamma = 1.0, f = 20$ Hz. (Online version in colour.)

generator is possibly made in performing C_3. To reveal the experiments under different $\dot{x}_1(0)$ with values following an approximate arithmetical sequence, we still hold this suspicious result in figure 14.

As indicated in [26], the mean drift velocity $\bar{v}_e$ will be significantly affected by the initial value of $\dot{x}_1(0)$. The value of $\bar{v}_e$ can be obtained by measuring the arc length in each experimental curve, then using it divided by the time interval in the drift motion. In terms of the values of $\bar{R}_e$ and $\bar{v}_e$, the period of the circular orbit is given by $\bar{T}_e = 2\pi\bar{R}_e/\bar{v}_e$. Figure 15 shows the values of $\bar{T}_e$ versus those of $\dot{x}_1(0)$ in the five cases. Clearly, except for case C_3, $\bar{T}_e$ linearly decreases as $\dot{x}_1(0)$ increases.

(c) Numerical investigations related to three-dimensional experiments

To compare the experimental results with the numerical ones, a deterministic initial state should be specified to the dimer. To simplify simulations, we neglect the dynamics of the rolling stage of the dimer on the groove, and specify the initial state of the dimer to be approximately characterized as $\mathbf{q}(0) = (0, 0, r + A_z \sin\phi_0, 0, \beta_0, 0)^{\mathrm{T}}$, $\dot{\mathbf{q}}(0) = (\dot{x}_1(0), 0, 0, 0, 0, 0)^{\mathrm{T}}$, where β_0, ϕ_0 and $\dot{x}_1(0)$ are the initial values of the dip angle, the vibration phase and the horizontal velocity of the dimer, respectively.

Basically the initial state specified to simulations cannot precisely coincide with the full scenario in our experiments. However, numerical findings in [26] indicated that the initial state essentially has little effect on the radius of the circular orbit, though the value of $\dot{x}_1(0)$ has an

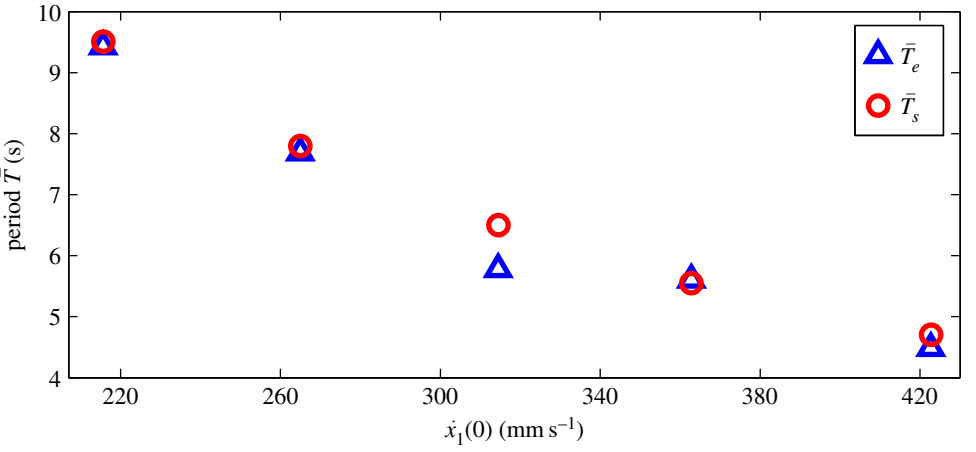

Figure 15. Experimental and numerical results for the period $\bar{T}$ of D-IV versus $\dot{x}_1(0)$. $\Gamma = 1.0$, $f = 20$ Hz. (Online version in colour.)

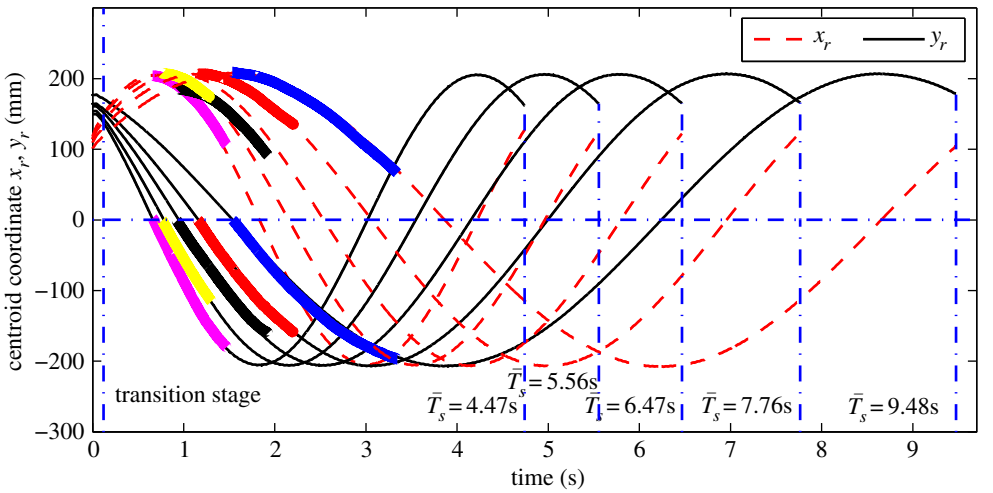

Figure 16. Experimental and numerical results for $x_r(t)$ and $y_r(t)$ of dimer D-IV in the cases from C_1 to C_5. Different colours mark the same meaning as in figure 14. $\beta_0 = 30^\circ$, $\phi_0 = \pi/6$, $\Gamma = 1.0$ and $f = 20$ Hz. (Online version in colour.)

impact on the mean drift velocities. In addition, under the same Γ and e, only the values of β_0 and ϕ_0 are responsible for the excitation of a drift mode. These peculiar property of dimer's motion in a stable drift mode allows the simulations to be advanced by the initial states with three adjustable parameters $(\beta_0, \phi_0, \dot{x}_1(0))$.

We assign $\beta_0 = 30^\circ$ based on the inclined angle of the groove relative to the horizontal plane (figure 2). Under the given values of Γ, e and β_0, numerical investigations indicate that a three-dimensional drift mode can be excited as $\phi_0 = \pi/6$ (the value is not unique). On the basis of the arithmetical sequence designated to $\dot{x}_1(0)$, together with fitting, good agreements between our numerical and experimental results can be achieved when the values of $\dot{x}_1(0)$ from C_1 to C_5 are modified as $\dot{x}_1(0) = 0.2156, 0.2650, 0.3145, 0.3628, 0.4227\,\mathrm{m\,s^{-1}}$, respectively.

Based on the initial states and the physical parameters shown in tables 2 and 3, figure 16 shows the curves of $x_r(t)$ and $y_r(t)$ versus time for the five different cases. After a transition stage within a very short time interval, all the curves follow the shape of a harmonic function with a nearly same

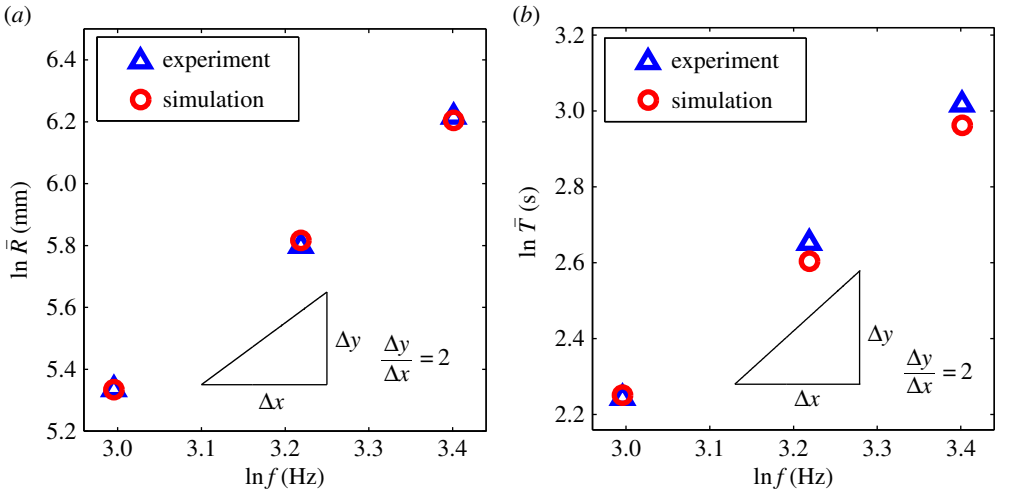

Figure 17. A ln–ln plot for the evolutions of (*a*) the radius $\bar{R}$, and (*b*) the period $\bar{T}$, versus frequency f: $\Gamma = 1.0$, $\dot{x}_1(0) = 0.2156\ \mathrm{m\,s^{-1}}$, $\beta_0 = 30^\circ$, $\phi_0 = \pi/6$. (Online version in colour.)

amplitude but different periods. This confirms that the mass centre of the dimer with different velocities drifts on a nearly same circular orbit. Figure 16 also shows the experimental curves marked online by different colours for the five cases. By the numerical results, the equivalent radius $\bar{R}_s$ and period $\bar{T}_s$ are also computed, and, respectively, shown in figures 14 and 15. Except for case C_3, they can always agree with the corresponding experimental results.

(d) Investigations for other properties of the circular orbit

To investigate the effects of frequency on the property of the circular orbit, we test dimer D-IV under different driving parameters: f takes three different values of 20, 25 and 30 Hz, while $\Gamma = 1$ is kept unchanged. For all the three experimental cases, the dimer initially lies on the position of the groove as the same one in case C_1. Namely, the value of $\dot{x}_1(0) = 0.2156\ \mathrm{m\,s^{-1}}$ remains unchanged in all three cases.

Figure 17 presents the ln–ln plots of the equivalent radius and period versus f. Besides good agreements between our numerical and experimental results, the slope of the line traced by the discrete points is nearly equal to 2. This confirms that both the radius and period of the circular orbit are nearly proportional to f^2, agreeing with our numerical findings given in [26].

6. Conclusion

In this paper, we have performed combined investigations of experiments and simulations for dimers bouncing on a vertically oscillating plate. Experimental investigations are implemented via a stereoscopic vision method with a pair of high-speed cameras to perform accurate measurements. Numerical simulations are carried out according to an existing numerical model recently developed in [25].

The combined investigations present experimental and numerical results in good agreements, and describe the dimer's dynamics in detail. Within a stable drift mode in both two- and three-dimensional situations, the dimer moves in various contact states including 'FM', 'SI', 'SC' and 'DI', forming a sequence in each cycle. This sequence evolves periodically accompanying the vibration. The dimer harvests the external energy mainly through a crucial event of DI occurring

at a fixed phase of the plate naturally selected by the dimer's dynamics, while the subsequent sequence of SIs at the staying ball modulates the energy to allow the dimer to approach a stable drift mode. Friction in these contact states is responsible for the formation of the asymmetric structures of the variables relevant to the dimer's horizontal motion. A transport behaviour can then appear in the trajectories of the mass centre of the dimer, following a circular orbit and a straight line in three- and two-dimensional scenarios, respectively.

By changing driving conditions, we test the two- and three-dimensional drift motions of dimers with different shapes. Through the combined investigations of simulations and experiments, we conclude as follows: Both the dimer's shape and the frequency of vibration are the significant factors of influencing the shape of the trajectory of the horizontal transport; the coefficient of restitution e and the vibration amplitude (often scaled by Γ) are the important factors responsible for the excitation of a periodic mode.

For the three-dimensional drift motion in a circular orbit, we find that both the orbit radius and period are approximately proportional to f^2, agreeing with our recent numerical discoveries [26]. In addition, similarity exists between the normal motions of the dimer and the fundamental bouncing-ball system. This means that further quantification of the mechanism underlying the dimer's transport behaviours is possible, though the various contact states complicate the dimer's dynamics. The study presented in this paper may help understand the intriguing phenomena exhibited in granular systems and a variety of mechanical vibrating systems.

Funding statement. This work was performed under the support of the National Natural Science Foundation of China (NSFC: 11132001).

Appendix A. Matrices for the dimer's dynamics

This appendix lists the forms of some matrices used in equation (2.1) for the dynamics of the dimer system:

$$\boldsymbol{M}(\mathbf{q}) = \begin{bmatrix} m & 0 & 0 & M_{14} & M_{15} & 0 \\ 0 & m & 0 & M_{24} & M_{25} & 0 \\ 0 & 0 & m & 0 & \frac{1}{2}mlc_\beta & 0 \\ M_{14} & M_{24} & 0 & M_{44} & 0 & J_2 s_\beta \\ M_{15} & M_{25} & \frac{1}{2}mlc_\beta & 0 & M_{55} & 0 \\ 0 & 0 & 0 & J_2 s_\beta & 0 & J_2 \end{bmatrix}, \tag{A 1}$$

where $M_{14} = -\frac{1}{2}mlc_\beta c_\theta$, $M_{15} = \frac{1}{2}mls_\beta s_\theta$, $M_{24} = -\frac{1}{2}mlc_\beta s_\theta$, $M_{25} = -\frac{1}{2}mls_\beta c_\theta$, $M_{44} = (\frac{1}{4}ml^2 + J_1)c_\beta^2 + J_2 s_\beta^2$, $M_{55} = \frac{1}{4}ml^2 + J_1$, m is the total mass of the dimer, and J_1, J_2 are, respectively, the principal inertias of the dimer with respect to its mass centre, $s_{(\cdot)}$ and $c_{(\cdot)}$ are, respectively, the abbreviations for sine and cosine functions, for example, s_β means $\sin\beta$, and so on.

$$\boldsymbol{W}(\mathbf{q}) = \begin{bmatrix} 0 & 0 & 1 & 0 & 0 & 0 \\ 0 & 0 & 1 & 0 & lc_\beta & 0 \end{bmatrix}^{\mathrm{T}}, \tag{A 2}$$

$$\boldsymbol{N}(\mathbf{q}) = \begin{bmatrix} 1 & 1 & 0 & 0 \\ 0 & 0 & 1 & 1 \\ 0 & 0 & 0 & 0 \\ 0 & -lc_\theta c_\beta & 0 & -ls_\theta c_\beta \\ -rs_\theta & (ls_\beta - r)s_\theta & rc_\theta & (r - ls_\beta)c_\theta \\ -rc_\theta c_\beta & -rc_\theta c_\beta & -rs_\theta c_\beta & -rs_\theta c_\beta \end{bmatrix}, \tag{A 3}$$

$$\boldsymbol{h}(\mathbf{q},\dot{\mathbf{q}},t)=\begin{bmatrix} -\frac{ml}{2}(c_\beta s_\theta(\dot\theta^2+\dot\beta^2)+2s_\beta c_\theta\dot\theta\dot\beta) \\ \frac{ml}{2}(c_\beta c_\theta(\dot\theta^2+\dot\beta^2)-2s_\beta s_\theta\dot\theta\dot\beta) \\ \frac{ml}{2}s_\beta\dot\beta^2 \\ \left(\left(2J_1-2J_2+\frac{ml^2}{2}\right)s_\beta\dot\theta-J_2\dot\gamma\right)c_\beta\dot\beta \\ -\left(\left(J_1-J_2+\frac{ml^2}{4}\right)s_\beta\dot\theta-J_2\dot\gamma\right)c_\beta\dot\theta \\ -J_2c_\beta\dot\theta\dot\beta \end{bmatrix} \tag{A 4}$$

and

$$\mathbf{Q}(\mathbf{q})=[0\quad 0\quad -mg\quad 0\quad -\tfrac{1}{2}mglc_\beta\quad 0]^{\mathrm{T}}. \tag{A 5}$$

References

1. Blair DL, Neicu T, Kudrolli A. 2003 Vortices in vibrated granular rods. *Phys. Rev. E* **67**, 031303. (doi:10.1103/PhysRevE.67.031303)
2. Aranson IJ, Tsimring LS. 2003 Model of coarsening and vortex formation in vibrated granular rods. *Phys. Rev. E* **67**, 021305. (doi:10.1103/PhysRevE.67.021305)
3. Goldhirsch I, Zanetti G. 1993 Clustering instability in dissipative gases. *Phys. Rev. Lett.* **70**, 1619–1622. (doi:10.1103/PhysRevLett.70.1619)
4. Mullin T. 2000 Coarsening of self-organized clusters in binary mixtures of particles. *Phys. Rev. Lett.* **84**, 4741–4744. (doi:10.1103/PhysRevLett.84.4741)
5. Burtally N, King PJ, Swift MR. 2002 Spontaneous air-driven separation in vertically vibrated fine granular mixtures. *Science* **295**, 1877–1879. (doi:10.1126/science.1066850)
6. Clement E, Rajchenbach J. 1991 Fluidization of a bidimensional powder. *Europhys. Lett.* **16**, 133–138. (doi:10.1209/0295-5075/16/2/002)
7. Ottino JM, Khakhar DV. 2002 Open problems in active chaotic flows: competition between chaos and order ingranular materials. *Chaos* **12**, 400–407. (doi:10.1063/1.1468247)
8. Pfeiffer F, Glocker C. 2000 *Multibody dynamics with unilateral contacts*. New York, NY: Wiley.
9. Holmes PJ. 1982 The dynamics of repeated impacts with a sinusoidally vibrating table. *J. Sound Vibr.* **84**, 173–189. (doi:10.1016/S0022-460X(82)80002-3)
10. Kowalik ZJ, Franaszek M, Pieranski P. 1988 Self-reanimating chaos in the bouncing-ball system. *Phys. Rev. A* **37**, 4016–4022. (doi:10.1103/PhysRevA.37.4016)
11. Mehta A, Luck JM. 1990 Novel temporal behavior of a nonlinear dynamical system: the completely inelastic bouncing ball. *Phys. Rev. Lett.* **65**, 393–396. (doi:10.1103/PhysRevLett.65.393)
12. Gilet T, Vandewalle N, Dorbolo S. 2009 Completely inelastic ball. *Phys. Rev. E* **77**, 055201(R). (doi:10.1103/PhysRevE.79.055201)
13. Barroso JJ, Carneiro MV, Macau EEN. 2009 Bouncing ball problem: stability of the periodic modes. *Phys. Rev. E* **79**, 026206. (doi:10.1103/PhysRevE.79.026206)
14. Frette V, Christensen K, Malthe-Sørenssen A, Feder J, Jøssang T, Meakin P. 1996 Avalanche dynamics in a pile of rice. *Nature* **379**, 49–52. (doi:10.1038/379049a0)
15. Wright HS, Swift MR, King PJ. 2008 Migration of an asymmetric dimer in oscillatory fluid flow. *Phys. Rev. E* **78**, 036311. (doi:10.1103/PhysRevE.78.036311)
16. Pacheco-Martinez HA, Liao L, Hill RJA, Swift MR, Bowley RM. 2013 Spontaneous orbiting of two spheres levitated in a vibrated liquid. *Phys. Rev. Lett.* **110**, 154501. (doi:10.1103/PhysRevLett.110.154501)
17. Atwell J, Olafsen JS. 2005 Anisotropic dynamics in a shaken granular dimer gas experiment. *Phys. Rev. E* **71**, 062301. (doi:10.1103/PhysRevE.71.062301)
18. von Gehlen S, Evstigneev M, Reimann P. 2009 Ratchet effect of a dimer with broken friction symmetry in a symmetric potential. *Phys. Rev. E* **79**, 031114. (doi:10.1103/PhysRevE.79.031114)
19. Dorbolo S, Volfson D, Tsimring L, Kudrolli A. 2005 Dynamics of a bouncing dimer. *Phys. Rev. Lett.* **95**, 044101. (doi:10.1103/PhysRevLett.95.044101)

20. Liu C, Zhao Z, Brogliato B. 2008 Frictionless multiple impacts in multibody systems. I. Theoretical framework. *Proc. R. Soc. A* **464**, 3193–3211. (doi:10.1098/rspa.2008.0078)
21. Zhao Z, Liu C, Brogliato B. 2009 Planar dynamics of a rigid body system with frictional impacts. II. Qualitative analysis and numerical simulations. *Proc. R. Soc. A* **465**, 2267–2292. (doi:10.1098/rspa.2008.0520)
22. Zhao Z, Liu C, Brogliato B. 2008 Energy dissipation and dispersion effects in granular media. *Phys. Rev. E* **78**, 031307. (doi:10.1103/PhysRevE.78.031307)
23. Liu C, Zhang H, Zhao Z, Brogliato B. 2013 Impact–contact dynamics in a disc–ball system. *Proc. R. Soc. A* **469**, 20120741. (doi:10.1098/rspa.2012.0741)
24. Zhang H, Liu C, Zhao Z, Brogliato B. 2013 Energy evolution in complex impacts with friction. *Sci. China-Phys. Mech. Astron.* **56**, 875–881. (doi:10.1007/s11433-013-5061-1)
25. Wang J, Liu C, Zhao Z. 2014 Nonsmooth dynamics of a 3D rigid body on a vibrating plate. *Multibody Syst. Dyn.* **32**, 217–239. (doi:10.1007/s11044-013-9385-4)
26. Wang J, Liu C, Jia Y, Ma D. 2014 Ratchet rotation of a 3D dimer on a vibrating plate. *Eur. Phys. J. E* **37**, 1–13. (doi:10.1140/epje/i2014-14001-x)
27. Zhang H, Brogliato B, Liu C. 2013 Study of the planar rocking-block dynamics with Coulomb friction: critical kinetic angles. *J. Comput. Nonlinear Dynam.* **8**, 021002. (doi:10.1115/1.4007056)
28. Zhong H, Lee C, Su Z, Chen S, Zhou M, Wu J. 2013 Experimental investigation of freely falling thin disks. Part 1. The flow structures and Reynolds number effects on the zigzag motion. *J. Fluid Mech.* **716**, 228–250. (doi:10.1017/jfm.2012.543)
29. Zhang Z. 2000 A flexible new technique for camera calibration. *IEEE Trans. Pattern Anal. Mach. Intell.* **22**, 1330–1334. (doi:10.1109/34.888718)